High Speed Synchronous Reluctance Machines: Materials Selection and Performance Boundaries

Mauro Di Nardo, *Member, IEEE,* Gianvito Gallicchio, Marco Palmieri, *Member, IEEE,* Alessandro Marfoli, Giovanni Lo Calzo, Michele Degano, *Senior Member, IEEE,* Chris Gerada, *Senior Member, IEEE,* and Francesco Cupertino, *Senior Member, IEEE*

***Abstract*—This paper presents a comprehensive comparative design exercise of Synchronous Reluctance (SyR) machines considering different soft magnetic materials and a wide range of speeds. First, a general design methodology able to consider all the consequences of selecting different materials is presented. In fact, magnetic non-linearities, rotor structural limitations and the rise of both stator and rotor iron losses are all considered. The adopted design approach allows achieving optimal stator and rotor geometries balancing all these competitive multi-physics aspects and keeping constant the cooling system capability. Both silicon-iron (SiFe) and cobalt-iron (CoFe) alloys with optimized magnetic and mechanical performance are examined to assess the maximum capabilities achievable with a SyR machine technology. The adoption of CoFe alloys leads to machines that outperform the SiFe counterparts up to a certain speed, above which, machines with SiFe provide better performance. Indeed, in the lower speed range, the effect of the higher saturation flux density of the CoFe materials is dominant, while for higher design speeds, their higher iron losses and lower yield strength, with respect to the SiFe ones, make the latter more convenient. All the design considerations are finally validated by comparing the predicted performance with the experimental test results on a 6.5kW, 80krpm SyR machine prototype.**

***Index Terms*—Analytical design, finite element analysis (FEA), high speed, material selection, motor design, synchronous reluctance machines, soft magnetic material.**

I. Introduction

THE ever increasing variety of soft magnetic materials in terms of chemical compositions, manufacturing processes and thermal treatments makes the electrical machine design a challenging task [1]. The material selection is particularly important when designing high power density electrical machines where the constituent materials are pushed to the working limits in order to maximize their exploitation [2]. Indeed, transportation applications in the aerospace sector require impressively high power density levels in order to compete with the mechanical counterparts [3]. Similar challenges are faced by the automotive industry [4], although the electrical machine requirements are different.

M. Di Nardo, A. Marfoli, M. Degano and C. Gerada are with the Power Electronics and Machine Control Group, University of Nottingham, UK, e-mail: mauro.dinardo4@nottingham.ac.uk, alessandro.marfoli1@nottingham.ac.uk, michele.degano@nottingham.ac.uk, chris.gerada@nottingham.ac.uk

G. Gallicchio, M. Palmieri and F. Cupertino are with the Department of Electrical Engineering and Information Technology, Politecnico di Bari, Italy, e-mail: gianvito.gallicchio@poliba.it, marco.palmieri@poliba.it, francesco.cupertino@poliba.it

G. Lo Calzo is with the Power Electronics Hardware Design Group at Ferrari Spa, Italy, email: giovanni.localzo@gmail.com

Non-oriented cold-rolled carbon steel with different silicon content (SiFe) and alloys with different ratio of cobalt-iron (CoFe) are the main soft magnetic material families commercially available in a wide range of lamination thicknesses and thermal treatments [5]. The first one covers the majority of the market share while the second is mainly used in high power density applications given its higher cost (about one order of magnitude) and higher saturation flux density [6]. Along with the latter, magnetic permeability, iron losses and mechanical strength are the main performance indexes affecting the material selection.

Clearly, the soft magnetic material choice depends on the considered electrical machine topology and related needs. Regarding high-speed electrical machines, permanent magnet synchronous machines, induction motors and switched reluctance topologies could benefit from the adoption of high grade or thin gauge SiFe or CoFe materials [2], [7], [8]. The iron losses at the maximum operating frequency and the saturation flux densities are the main performance factors driving the choice of the soft magnetic material to be adopted. The yield strength also plays a fundamental role when designing high speed induction machines or interior permanent magnet synchronous with laminated rotor back iron [9], [10]. Regarding electrical machines for transportation applications, the material selection is also influenced by the maximum torque-speed profile along with the operating cycle [11]–[13].

Indeed, the driving cycle defines the material choice correctly balancing the competitive needs of having high saturation level, low iron losses and high yield strength [14]. The soft magnetic material selection is particularly challenging when designing high-speed electrical machines featuring complex rotor structure such as Synchronous Reluctance (SyR) machines. The latter have been historically employed in low-speed general purpose applications and are becoming more and more industrially accepted thanks to their superior performance in terms of efficiency when compared to induction motors [15], [16]. Their simple rotor construction and the capability to operate with a wide constant power speed range with the aid of low energy density magnets or small amount of rare-earth based magnets are further benefits justifying the automotive sector attention towards SyR machines [17]. The conflicting requirements between the rotor structural integrity at high speed and the electromagnetic and thermal performances severely influence the design process including the soft magnetic material selection [18]–[20]. A comparative study of low-speed SyR machines with different grades of SiFe has

been reported in [21] mainly assessing the efficiency aspects of the material choice. A FE-based design optimization procedure has been presented in [22] where the authors evaluate the SyR maximum power capability as function of the speed for different soft magnetic materials. Another interesting attempt to include the structural aspects within the design workflow has been presented in [23]. A linear analytical model based on the magnetic equivalent circuits has been used to identify the maximum power capability of SyR machines as function of the maximum design speed. Although these two studies attempt to asses the effect of the structural limitation on the electromagnetic performance, they both consider a fixed stator design and current density disregarding the thermal impacts of the increased iron losses. Indeed, if the cooling system is kept constant during the design exercise, as the speed increases the ratio between Joule and total losses has to decrease in order to maintain the same total losses and so approximately the same thermal behaviour. Otherwise a different cooling system has to be designed leading to an unfair comparison.

This paper presents a comprehensive design approach of high speed SyR machines leading to the full definition of both stator and rotor geometries considering the limitation introduced by the rotor structural behaviour and thermal constraints of the adopted materials and cooling system. The design exercise is then carried out considering different types of soft magnetic materials in order to assess the maximum power capability of this machine topology as function of the design speed. The proposed design approach is based on the works presented in [24], improved in [25]–[27] and implemented in [28]. In particular, the design routine suitable for high speed SyR machines presented in [26], is here extended in order to evaluate different stator and rotor soft magnetic materials. Along with the rotor structural limitations and the stator losses also the rotor iron losses are included in the design workflow. By doing so, it is possible to fairly asses the SyR performance boundaries achievable with the considered materials. After introducing the design procedure in section II, the soft magnetic material selection is discussed in section III. The results of the comparative design exercise are then reported in section IV highlighting the performance boundaries that each selected material can achieve as function of the design speed. The optimal performance and machine geometries are then analyzed in section V along with a thermal behaviour assessment. The proposed analysis and considerations are finally experimentally validated in section VI where several tests results are reported of a 6.5kW-80krpm SyR machine designed for an electrical assisted turbocharger [29].

II. Design Procedure

Considering a given outer machine envelope and cooling system capability, the performance of a SyR machine can be expressed as a function of two independent variables [24]: the split ratio (sr) and the magnetic ratio (mr). The first one is the ratio between the airgap diameter and the external stator one, whereas the latter is the ratio between the airgap flux density (B_g) and the iron flux density (B_{fe}). All the other geometrical quantities, which are reported in Fig. 1a, can be

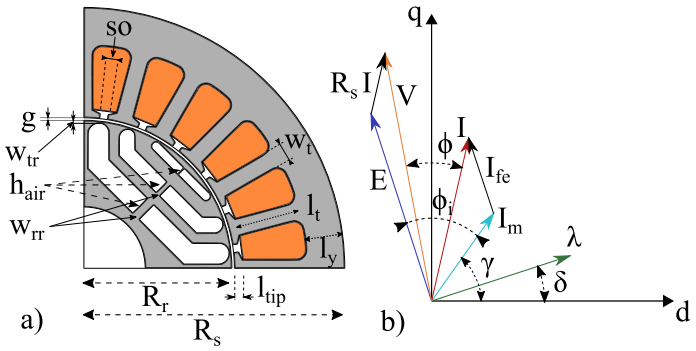

Fig. 1. a) Parametrization of the stator and rotor geometry. b) Vector diagram a SyR machine.

expressed in terms of these two variables. In the next sub-section, the main design equations are outlined, while in the last sub-section a computational efficient FE-based procedure to refine the analytically predicted performance is presented.

A. Analytical design equations

Both torque and power factor are investigated since their dependency from the design variables sr and mr is different. In fact, the torque depends both on inductances and machine capability to produce the stator m.m.f. and flux, whereas the power factor only on the d- and q-axis inductances.

Indeed, the torque can be calculated as:

$$T = \frac{3}{2} p(\lambda_d i_q - \lambda_q i_d) \tag{1}$$

where p is the number of pole pairs, i_d and i_q are the d- and q-axis currents, whereas λ_d and λ_q are the d- and q-axis flux linkages which can be written as follows:

$$\lambda_d = (L_{dm} + L_s) i_d + L_{dq} i_q \tag{2}$$

$$\lambda_q = L_{dq} i_d + (L_{qm} + L_s + L_{q-rib}) i_q \tag{3}$$

where the term L_{dq} takes into account the cross-coupling effects which are neglected in the first step of the design process. The d- and q-axis inductances are the sum of the magnetizing (L_{dm} and L_{qm}) and leakage components where L_s is the leakage inductance, equal for both axes, while L_{q-rib} is the additional leakage inductance due to the shunted flux via the iron ribs.

The power factor can be deduced from the steady-state vector diagram reported in Fig. 1b, in which λ is the flux linkage, I_m is the magnetizing current, I_{fe} takes into account the iron losses, E is the electromotive force, R_s and V are the stator resistance and voltage respectively and I is the total stator current. If the influence of the stator winding and equivalent iron losses resistances are neglected, the power factor pf coincides with the so-called internal power factor ipf, defined as the cosine of the angle between the induced voltage E and the current I_m vectors.

By defining the d-axis flux per pole ($2R_r L B_g$), the tooth width and stator yoke radial thickness can be evaluated given a certain iron flux density B_{fe}. Considering a uniform distribution of the equivalent rotor slots and imposing barriers

having the same permeance and the total iron thickness along the q-axis equal to the stator yoke thickness, allows fully defining the rotor geometry [24]. The magnetizing components of both d- and q-axis inductances and the leakage inductance (L_{dm}, L_{qm}, L_s) can be then calculated as function of the design variables sr and mr, as in [24], [25].

The d-axis current component can be deduced from the Ampere's law (when $i_q = 0$) [26] while the q-axis component can be calculated knowing i_d and the maximum current I_{max}. The latter depends on the cooling capability k_{cool} (in terms of W/m^2) and geometric parameters, as reported in (4):

$$I_{max} = \frac{1}{3N}\sqrt{\frac{k_{fill}A_{slots}}{2\rho(L+L_{ew})}(2\pi R_s L k_{cool} - P_{fe})} \quad (4)$$

where k_{fill} is the filling factor of the slot, A_{slots} is the slots area, R_s is the outer radius of the machine, ρ is the copper resistivity, L and L_{ew} are the axial winding and the end-winding lengths. The above maximum current calculation is based on the conservative hypothesis that Joule and iron losses (P_{fe}) of both stator and rotor are dissipated via the stator cooling system. The assumption of considering constant total losses determines a reduction of the torque capability as the maximum speed requirement increases. In fact, the torque derating is correlated to the reduction of copper losses in order to balance the extra iron losses at high speed. Therefore, the cooling system can be considered invariant as the speed requirement increases. Further thermal considerations will be provided in section V-C. The iron losses are estimated using (5):

$$P_{fe} = k_{fe}M_{fe}[k_h f^{\alpha} B_{fe}^{\beta} + k_e(fB_{fe})^2] \quad (5)$$

where k_{fe} is an empirical coefficient, M_{fe} is the iron mass, k_h and k_e are the hysteresis and the eddy current coefficients respectively, α and β are exponential coefficients for the frequency and the flux density respectively, and f is the electrical frequency.

The torque capability is also reduced by the rise of the structural rib thickness which increases with the centrifugal forces affecting the rotor flux guides. The selection of the iron ribs thickness, position and orientation along each barrier can only be accurately performed via a structural FE study. However, a simplified analytical formulation considering only the steady state centrifugal force $F_c(i)$ acting on the i^{th} flux guide is usually adopted [22], [30] to estimate the total iron rib $w_{rib}(i)$ of the i^{th} barrier:

$$w_{rib}(i) = \frac{k_s F_c(i)}{\sigma_s L} = \frac{k_s}{\sigma_s L} m_{fg}(i) R_{fg}(i) \omega_m^2 \quad (6)$$

In (6), k_s is a safety factor, σ_s is the yield strength of the rotor lamination, m_{fg} is the sum of the flux guide masses which are sustained by the i^{th} iron bridge, R_{fg} is the center of gravity of the same masses, and ω_m is the mechanical speed. Once the total rib thickness per each barrier is calculated, its optimal distribution along the flux barrier can be identified with a structural FEA [27]. However, wherever the iron ribs are located along the flux barrier, it can be assumed that they electromagnetically act in the same way in terms of average torque. In other words, the torque reduction due to the iron ribs mainly depends on their size and not on their distribution and position along the flux barriers. Considering n barriers per pole and supposing that the deterioration of the performance is proportional to the average value of the iron ribs w_{avg} (7):

$$w_{avg} = \frac{1}{n}\sum_{i=1}^{n} w_{rib}(i) \quad (7)$$

then the rib shunted q-axis flux λ_{rib} can be approximated as in (8), assuming that all the ribs share the same saturation level (B_{sat}):

$$\lambda_{rib} = \frac{4}{\pi} N_s k_w w_{avg} L B_{sat} \quad (8)$$

The increment of the q-axis inductance can be then calculated allowing to estimate the worsening of both torque and power factor due to the structural iron ribs.

The described design procedure has been applied to a case study whose details are reported in Table I. The dependencies of main performance indexes from the split and magnetic ratios are analyzed by contour plots shown in Fig. 2a1-f1 for a design speed of 60 krpm. The same sub-figures report the results of transient FEAs highlighting the limits of the analytical formulations. Indeed, constant torque (Fig. 2a1) and power factor loci (Fig. 2b1) show considerable mismatches between the analytical and the FEA results.

Fig. 2c1 reports a comparison between the estimated stator iron losses and the FE computed ones. Clearly, the former do not match with the FE computation, both in quantitative and qualitative terms. This mismatch is mainly due to the non-uniform distribution of the flux density within the machine.

The analytical and FE calculation of the d-axis inductance L_{dm} is shown in Fig. 2d1. It can be noticed that saturation of the d-axis greatly reduces the d-axis inductance, leading to a worse estimation of torque and power factor. Fig. 2e1 confirms that approximating the increment of the q-axis inductance proportional to the average total bridge is acceptable, since the analytical contours clearly match the FE ones. Fig. 2f1 reports the ratio between $L_{dq}i_q$ and $L_{dd}i_d$, which quantifies the cross-coupling effect. As expected, in the design plane region where the cross coupling is more pronounced, the torque and power factor error is higher.

TABLE I
MACHINE PARAMETERS

Parameter	Value	Units
Outer stator radius	30	mm
Stack length	30	mm
Pole pair	2	/
Stator slots	24	/
Airgap thickness	0.3	mm
Cooling system	Spiral water jacket	/
Cooling capability	50000	W/m^2
Iron flux density	1.4	T
N° of flux barriers	3	/
Shape of flux barriers	U/I-shaped	/

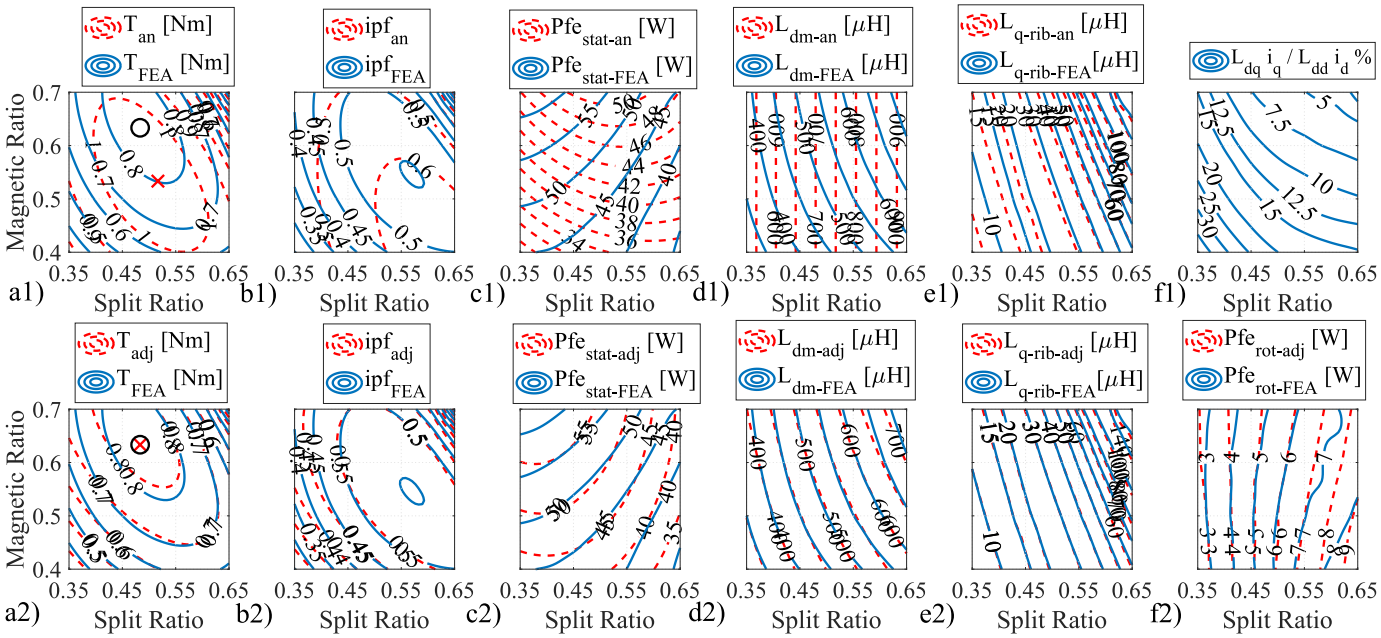

Fig. 2. Comparison between analytical and FE computed torque (a), power factor (b), stator iron losses (c), d-axis magnetizing inductance (d), q-axis ribs inductance (e), if the FE-adjustment is not enabled (1) and if it is enabled (2). f1) Cross coupling effects, f2) adjusted rotor losses vs FE rotor losses.

B. Bridging the analytical design gaps

Despite the advantage of the fast performances evaluation, the pure analytical design approach shows evident accuracy limits in the performance estimation. These are mainly due to the disregarded or approximated aspects of the analytical modelling, such as the saturation of the d-axis, the cross-coupling effects and the estimation of the iron losses. In order to properly consider all the aforementioned design aspects, a comprehensive procedure able to adjust the analytical-FE mismatch due to the saturation effects, increased iron losses and iron ribs incurring at high speed, has been proposed in [26]. Such adjustment procedure is here extended in order to include the evaluation of the rotor iron losses needed to determine the maximum current. The analytical design procedure described in the previous sub-section is first carried out for the whole $sr - mr$ plane. Then, for each machine placed at the corners of the design plane, an iterative FE procedure is performed in order to accurately identify the iron losses (and so the rated current) and all the inductance components. The proposed procedure is summarized in the flowchart in Fig. 3 and consists in the following steps.

- At the first step, the maximum current is calculated using (4) and the analytical estimation of the stator iron losses.
- Then, a transient non-linear FEA is carried out to calculate both stator and rotor iron losses, allowing to evaluate the mismatch with the analytical values.
- If the relative error is less than a predefined threshold, the algorithm proceeds to the next step. Conversely, the iron losses (both the stator and rotor ones) are updated and a new maximum current is calculated.
- Once the correct i_d, i_q currents are identified, a couple of linear FEAs are carried out with the permeability frozen to the values obtained from the previous non-linear FE simulation. The first linear FEA is done supplying only with the d-axis current, while the second with only the q-axis component. By doing so, it is possible to split both d- and q-axis inductances into two components allowing also the characterization of the cross coupling term. A further subdivision of the inductances is also performed calculating the magnetizing components integrating the airgap flux density.
- The correction factors can be then calculated as the ratio between the finite element ($_{FEA}$) and the analytical ($_{AN}$) prediction:

$$k_x^i = \frac{x_{FEA}^i}{x_{AN}^i} \tag{9}$$

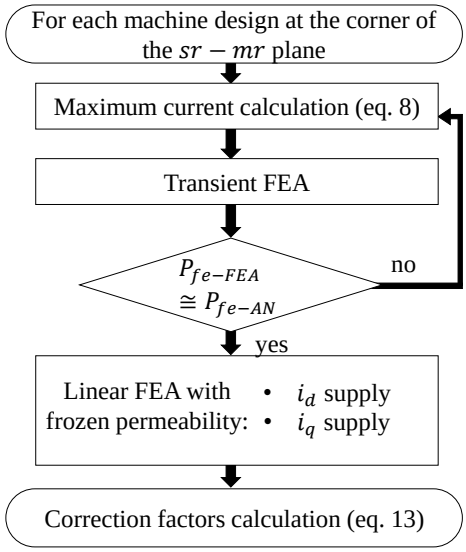

Fig. 3. Flowchart for the correction factors identification.

where x can be either the iron losses P_{fe}, the magnetizing inductances L_{dm}, L_{qm}, the slot leakage inductance L_s or the cross coupling inductance L_{dq} of the i^{th} corner machine.

Once all the corner solutions of the design plane $sr - mr$ are identified with the procedure summarized above, all the correction factors can be extended to the whole $sr - mr$ plane with a linear interpolation (i.e. defining the function $k_x(sr, mr)$). Finally, torque and internal power factor of each machine in the design plane $sr - mr$ can be re-calculated adjusting the inductance components and the iron losses with the respective interpolated correction factors ($k_x(sr, mr)$).
Fig. 2a2-f2 report the results of the proposed hybrid design procedure along with the FE estimated performance.

The good agreements of torque and power factor (Fig. 2a2-b2) is clearly due to the reliable estimation of the d-axis inductance (Fig. 2d2), and the stator and rotor iron losses (Fig. 2c2-f2).

III. Materials selection

The performance and optimal geometry of a high speed SyR machine heavily depends on the selected soft magnetic material. In fact, specific iron losses p_{fe} and yield strength σ_s are intrinsic characteristics of the material affecting the decrement of the performance as the speed increases: the former reduces the maximum current, whereas the latter increases the q-axis inductance. Obviously, it is possible to achieve the best performance adopting a material with low specific iron losses and high yield strength. Unfortunately, materials with high σ_s generally present high specific iron losses and viceversa. Indeed, high mechanical strength is achieved by reducing the grain size of the material which in turn increases the iron losses [31]. Therefore, the choice of the lamination material is the result of a comparative study in which materials with different magnetic and mechanical properties are analyzed. The best solution, i.e. the one which guarantees the maximization of the output power for a defined rotor speed, will depend on the material characteristics.
Fig. 4 reports a comparison in terms of yield strength, saturation flux density and iron losses of some commercially available grades of SiFe (•, ★, ▼, ■) and CoFe (▲ and ♦) under their respective trade names. The iron losses have been calculated with a modified Steinmetz model (eq. (5)) with the coefficients fitted with the data provided by the manufacturers [32]–[35]. The saturation flux density is considered as the point where a 5% flux density improvement corresponds to a 50% increment of the magnetic field.
Common SiFe steels (• in Fig. 4), such as M250 and M330 with 0.35/0.5mm lamination thickness are usually used in medium-high performance volume-manufactured machines [36] thanks to their medium electromagnetic and mechanical characteristics. Reducing the lamination thickness (from the more common range 0.35-1mm to 0.1-0.2mm) of standard SiFe alloys (with Si content around 3%) is a commonly adopted approach to lower the eddy current losses (e.g. NO10, NO20, Arnon 7, ★ in Fig. 4). Reducing the lamination thickness is a less expensive way leading to higher flux densities with respect to the option of increasing the Si content even though it slightly complicates the assembly process [5]. It is well known that the silicon (Si) addition to the carbon steel increases the electric resistivity and the mechanical hardness at the cost of a lower saturation flux density and permeability [37]. The maximum Si content has been historically limited to 3.5% by manufacturing considerations since higher percentages make the alloy more brittle and hard and so difficult and expensive to produce. In the last decade, this challenge has been overcome thanks to the adoption of tailored manufacturing processes such as chemical vapor deposition [38] and diffusion annealing [39] (e.g. 10JNEX900 and 10JNHF600, ▼ in Fig. 4) pushing the maximum Si content up to 6.5% [40]. Extremely high yield strength (above 800 MPa) has been achieved with special production techniques (e.g. dislocation strengthening [41]), at the cost of increased iron losses (e.g. 35HXT780T, ■ in Fig. 4).
The cobalt content makes the CoFe alloys more expensive than the SiFe contender but allows higher saturation flux densities. In general, CoFe alloys have lower yield strength with respect to SiFe (i.e. Vacoflux 48, Vacoflux 50 and Hiperco 50A, ▲ in Fig. 4). This metric can be improved by lowering the Co content (e.g. Vacoflux 17, Hiperco 27) or by adding small percentage of vanadium and/or by additional alloying the material with niobium (Hiperco 50HS, Vacodur 49 and Vacodur S Plus, ♦ in Fig. 4), all at the cost of higher iron losses and lower saturation levels [36]. However, the most important leverage to control the trade-off between mechanical and electromagnetic performance of CoFe alloys is the annealing process. Lower annealing temperatures decrease the grain sizes leading to higher yield strength and lower electromagnetic properties (e.g. Hiperco 50HS, Vacodur 49 mec, Vacodur S Plus in Fig. 4). By doing so, stators and rotors can be manufactured from the same material and then be subject to different heat treatments in order to achieve a magnetically optimized stator and a rotor with a higher yield strength. It is worth to underline that the cutting process of laminated materials worsens the electromagnetic performance [42]. However, SiFe alloys could and are usually used without expensive post manufacturing thermal treatments, which would restore part of this magnetic property deterioration [43]. On the contrary, for CoFe alloys, the annealing process is indispensable to obtain the desired magnetic and mechanical characteristics [5].

The above considerations reveal the rationale behind the manufacturers' common choices of adopting SiFe alloys, with standard Si content, in low-medium power density applications and/or high volume electrical machines production. On the contrary, CoFe alloys are relegated to niche applications (e.g. aerospace and motor sport) where the higher power density benefit, allowed by the higher saturation levels, outweighs the higher cost [3].
Analysing Fig. 4, it is already possible to envisage the lack of an absolute winner, i.e. a soft magnetic material outperforming the others for every design speed. In fact, the relative vertical positions of the considered materials change as the frequency increases.
With the aim of analysing a wide range of materials, five different steel grades have been investigated for the comparative study shown in the next sections: a common SiFe grade

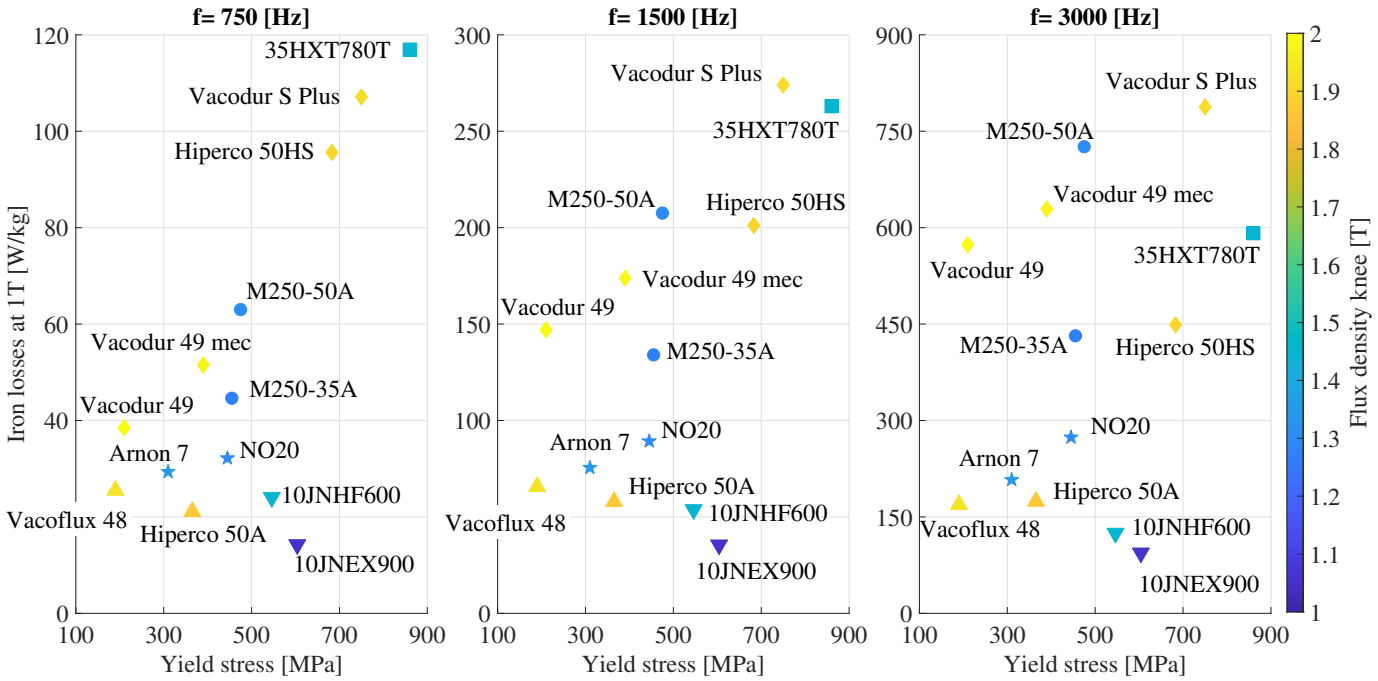

Fig. 4. Soft magnetic materials comparison: iron losses at 1 T at different frequencies (750, 1500, 3000 Hz) as function of the yield strength; the colored scale shows the knee flux density.

TABLE II
SELECTED LAMINATION MATERIALS

Name	Stator (S)	Rotor (R)	Thickness (S/R)
M1	M250-35A	M250-35A	0.35 / 0.35 mm
M2	10JNHF600	10JNHF600	0.1 / 0.1 mm
M3	10JNHF600	35HXT780T	0.1 / 0.35 mm
M4	Hiperco 50A	Hiperco 50A	0.15 / 0.15 mm
M5	Hiperco 50A	Hiperco 50HS	0.15 / 0.15 mm

(M250-35A), a high performance SiFe having low iron losses and good mechanical performance (10JNHF600), a SiFe alloys with outstanding yield strength (35HXT780T) and two CoFe alloys (Hiperco 50A, Hiperco 50HS). Table II summarizes the stator-rotor sets of materials considered: three combinations feature the same materials for both stator and rotor, while the other two have materials optimized magnetically for the stator and mechanically for the rotor.

IV. Performance Boundaries

The design procedure described in section II is applied in the following for the machine parameters reported in Table I. Several maximum speed requirements (from 0 to 120 krpm) and the material combinations listed in Table II are explored. In order to maximize the magnetic exploitation of each material, all the machines have been designed considering iron flux densities (stator and rotor yokes and stator teeth) proportional to the flux density at the knee of the respective BH curve. In particular, the stator and rotor yokes flux densities have been set equal to the knee flux density, whereas the stator tooth one is assumed to be 20% higher.

Fig. 5a reports the torque of the optimal designs in the $sr-mr$ planes for each design speed and for all the considered soft magnetic materials. Fig. 5b shows the power factor of the same designs. It is worth to underline that the optimal design for a given speed and combination magnetic materials is hereafter considered as the one providing the maximum torque in the plane $sr-mr$. Fig. 2a2 reports the location of the maximum torque design with a marker. Clearly, another design solution in the plane $sr-mr$ can be chosen (e.g. the one providing the maximum internal power factor). However, the maximum torque selection criterion has been adopted because the aim of this comparative design exercise is to asses the performance boundaries of SyR machine topology in terms of output power as function of the speed and magnetic materials.

Fig. 5a and b show the good match between the performance estimated with the proposed method and the FEA-calculated ones. As expected, torque and power factor decrease with the speed regardless of the alloy type.

All SiFe materials combinations start from the same torque values but, the standard one (M1) deteriorates with a higher rate with respect to the other two (M2, M3). On the contrary, the power factor of the optimal machines featuring the standard SiFe (M1) has a similar trend to the one achieved with the high grade SiFe (M2). Adopting SiFe alloy with optimized mechanical property on the rotor (M3) allows to improve both performance indexes but mostly the power factor. These improvements are even more evident for higher speeds.

CoFe steels outperform the SiFe contenders only up to a certain speed. It is worth to underline that the CoFe machines deteriorates more quickly than the SiFe ones both torque and power factor wise. Indeed, considering machines at 1 and 80 krpm, M2 (M3) torque worsens about 38% (34%) while M4

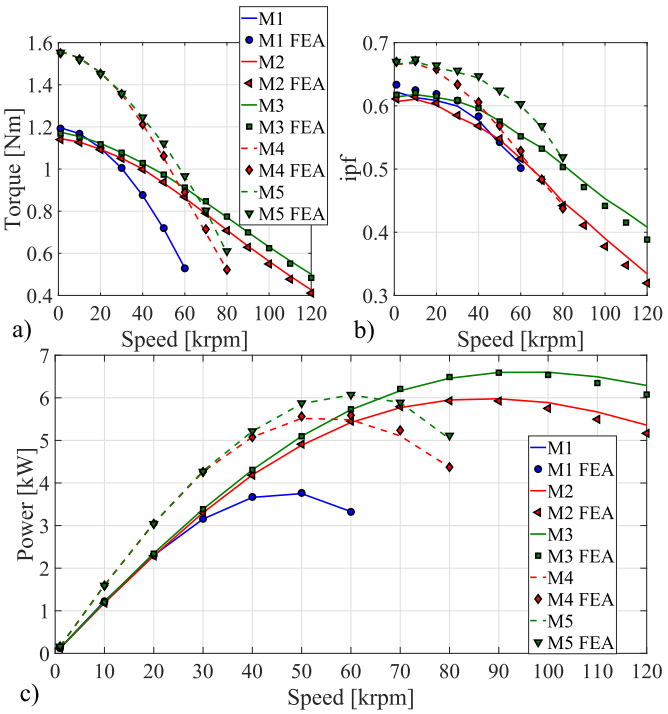

Fig. 5. Performance boundaries of the SyR machine technology, i.e. maximum achievable torque (a), internal power factor (b), and output power (c) as a function of the design speed for different soft magnetic materials.

(M5) 66% (61%). Similarly, the power factor decrements are about 26% and 17% for M2 and M3 and circa 33% and 22% for M4 and M5, respectively. The adoption of alloys with higher saturation levels, e.g. CoFe, leads to a higher q-axis flux leakage due to the structural ribs with respect to the SiFe cases. This is the main cause of the bigger rate of performance decrement of CoFe alloys with respect to the SiFe ones.

Fig. 5c reports the maximum output power as a function of the speed for all materials. Each considered material combination features a threshold speed above which it is not convenient to further increase the speed as a mean to push the output power and so the volumetric power density for a given cooling system. This threshold speed is clearly higher when adopting high performance SiFe alloys; for M1 this speed limit is 50 krpm, for M2 and M3 is about 90 krpm while M4 and M5 reach 50 and 60 krpm, respectively. The maximum output power is also approximately 10% higher when using high performance SiFe alloys (e.g. M2-6kW, M4-5.5kW) with respect to the CoFe ones. The adoption of standard SiFe allows reaching a maximum power 30% smaller than the more performing high grade SiFe M2. As previously stated, CoFe alloys outperform the SiFe ones up to a certain speed, circa 55 or 65 krpm (considering M4 and M5 respectively). The power gain is maximum around 40 krpm and it is about 17%. Above this speed, the power improvement decreases until it becomes negative around 55 and 65 krpm after which SiFe alloys are definitely more convenient. Adopting alloys with optimized mechanical performance for the rotor (e.g. M3 and M5) allows to improve the output power of almost 10% for both SiFe and CoFe alloys. This improvement is more evident at high speed levels where the iron ribs dimensions become significant and have a major effect on the overall performance.

V. Analysis of the Optimal Designs

The comparative design exercise, reported in the previous section, shows that the maximum speed requirement is crucial for the selection of the soft magnetic materials.
The optimal machine geometries change as the speed increases and vary according to the selected soft magnetic materials. In fact the location of the maximum torque design in the plane $sr - mr$ (highlighted with the marker in Fig. 5a2) changes with the speed and consequently also the optimal geometry changes. Fig. 6a and 6b report the split and the magnetic ratios of the torque-wise optimal machines as function of the speed. Their global trends are not affected by the chosen lamination material. In fact, both design variables decrease as the speed increases but the rate of decrement depends on the materials.

In the next sub-section, the optimal geometries are analyzed in details while in the sub-section V-B the rationale behind these trends is investigated separately evaluating the effects of the iron losses and iron ribs increments. A thermal assessment of the selected machines is finally reported in the sub-section V-C.

A. Optimal geometries

In Fig. 7, the cross sections of the optimal machines at four different speeds (20, 40, 80 and 120 krpm) and their flux density distribution at the rated condition are reported. As the speed increases the rotor radius always decreases, but machines featuring rotor materials with low yield strength (e.g. M2 and M4) present smaller rotors with respect to M3 and M5. Similarly, the decrement of the optimal magnetic ratio implies the reduction of the stator tooth (w_t) and yoke (l_y) as well as the rotor flux guide dimensions as reported in Table III. This decrement is again less pronounced when adopting a rotor lamination material with optimized mechanical performance. It is worth to underline that the selected optimal solutions for certain speeds and material combinations are definitely unconventional given the low split ratio and the high tooth length. These particular geometries could lead to manufacturing challenge, but from the electromagnetic point of view they provide the maximum torque. Selecting another solution in the $sr - mr$ plane, e.g. geometries with conventional proportions

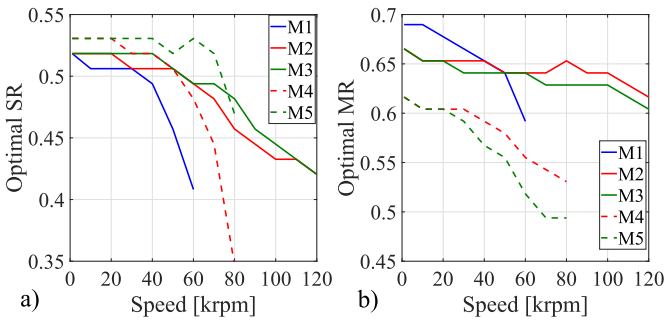

Fig. 6. Split (a) and magnetic ratios (b) of the optimal torque-wise machines as a function of the design speed.

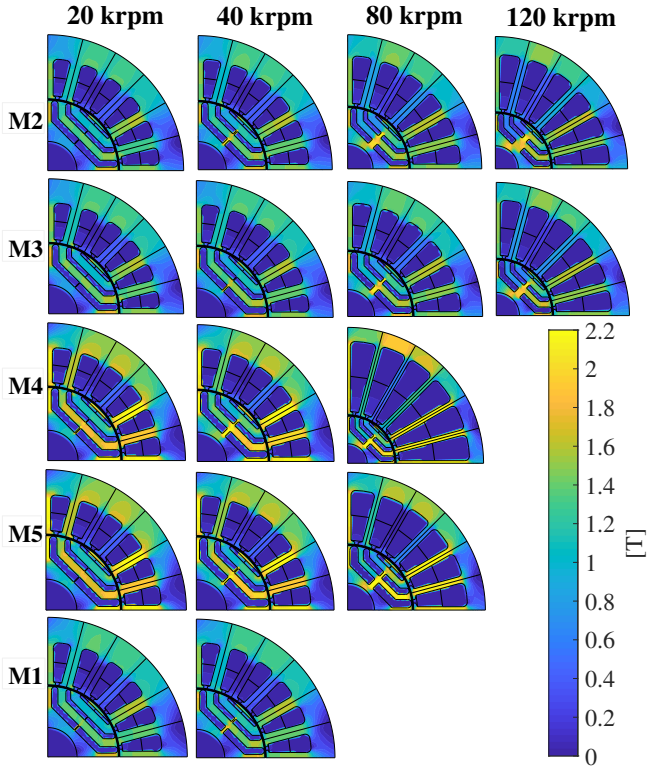

Fig. 7. Cross section of the optimal machines obtained for different lamination materials.

(and so smaller tooth length), would surely be sub-optimal given their lower torque production capability.

Table III also reports the average torque, the iron losses, the torque reduction due to the iron ribs and the maximum current reduction due to the iron losses. For each material combination, both percentage variations ($\Delta T_{rib}, \Delta I_{max}$) are calculated in relation to the respective values of the low speed designs (1000 rpm).

The iron losses in CoFe machines are always higher compared to the high performance SiFe ones (e.g. M2 and M3). At high speed, 80 krpm, this aspect heavily affects the average torque, via the reduction of the maximum current ΔI_{max} (see eq.(4)). However, at 40 krpm, the higher knee flux density of the CoFe steel compensates the reduction of the stator current due to the iron losses rise and so the torque is higher with respect to the corresponding SiFe machines.

It is also worth to notice that although the CoFe alloys have lower yield strengths, the torque reductions due to the iron ribs (ΔT_{rib}) are smaller with respect to the SiFe ones. This is mainly due to the fact that the optimal CoFe machines have a lower rotor radius.

B. Behind the boundaries

In this sub-section, the trends shown in Fig. 6 and so the optimal geometries are justified analysing the constant torque and power factor loci in the design plane $sr - mr$ for three different rotor speeds separately considering the structural and iron losses limiting factors. For the sake of brevity, only the most performing material combination above 65 krpm (i.e. M3) is shown and discussed as the others behave in a similar manner.

TABLE III
COMPARISON BETWEEN OPTIMAL MACHINES

Speed	Variable	M1	M2	M3	M4	M5
40 krpm	$T[Nm]$	0.87	1.00	1.03	1.21	1.25
	$P_{fe-st}[W]$	87.7	36.1	36.0	56.7	53.6
	$P_{fe-rot}[W]$	17.7	2.79	10.1	16.4	26.5
	$\Delta T_{rib}[\%]$	3.1	2.8	2.2	4.3	2.4
	$\Delta I_{max}[\%]$	20.7	7.01	8.40	13.81	15.22
	$w_t[mm]$	2.28	2.33	2.34	1.93	1.89
	$l_y[mm]$	5.06	5.18	5.21	5.10	5.00
	$h_{air-1}[mm]$	1.45	1.48	1.47	1.62	1.76
	$h_{air-2}[mm]$	1.05	1.08	1.14	1.17	1.28
	$h_{air-3}[mm]$	0.60	0.62	0.55	0.67	0.73
80 krpm	$T[Nm]$	-	0.71	0.77	0.52	0.60
	$P_{fe-st}[W]$	-	86.9	84.2	175.5	159.5
	$P_{fe-rot}[W]$	-	6.38	16.8	14.1	35.3
	$\Delta T_{rib}[\%]$	-	11.2	8.2	6.2	7.2
	$\Delta I_{max}[\%]$	-	18.1	19.7	42.5	44.1
	$w_t[mm]$	-	2.11	2.14	1.16	1.46
	$l_y[mm]$	-	4.68	4.75	3.06	3.85
	$h_{air-1}[mm]$	-	1.34	1.50	1.52	1.82
	$h_{air-2}[mm]$	-	0.97	1.09	0.91	1.32
	$h_{air-3}[mm]$	-	0.56	0.62	0.52	0.76

Fig. 8a, 8b and 8c show the constant torque loci calculated considering only the effect of the iron losses for three different speeds (1, 60, 120 krpm). As the speed increases, the maximum torque designs (■ @ 1 krpm, • @ 60 krpm, ♦ @ 120 krpm) move towards the bottom-right side of the $sr - mr$ plane, therefore the optimum split ratio increases whereas magnetic ratio decreases. This trend can be explained considering that the maximum torque location is a compromise between the needs of maximizing the machine anisotropy (L_d/L_q, Fig. 9a), the magnetizing current i_d (Fig. 9b) and the q-axis current i_q (Fig. 9c). For sake of brevity, Fig. 9 reports the contours only at 60 krpm together with the maximum torque locations for all the three speeds (1, 60 and 120 krpm). Indeed, the L_d/L_q and i_d are speed independent when the iron ribs are neglected while the q-axis current i_q is affected by the iron losses and so by the speed. As the speed increases, the higher iron losses lead to a q-axis current reduction (although the contour shape of i_q is not affected). Therefore, the maximum torque design moves towards the area of the design plane with lower stator and rotor iron losses (reported in Fig. 9d, e) and higher magnetic anisotropy (see Fig. 8a). Along the same direction, the internal power factor increases as shown in Fig. 9f because it follows the saliency ratio improvement. Fig. 10a, and 10b report the constant torque loci obtained considering only the iron ribs effect for two different speeds (60 and 120 krpm). As the speed increases, the maximum torque designs move towards the left because the lower the split ratio the lower the average total bridge w_{avg}, as reported in Figs. 10c for the 60 krpm case. In fact, lower rotor radius implies lower centrifugal forces, which reduce the iron rib thicknesses. It is worth to underline that the influence of the iron rib thickness is heavier on the

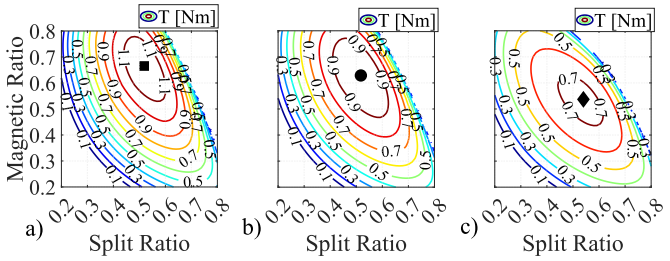

Fig. 8. Constant loci obtained considering only the losses effect. Torque at: (a) 1 krpm, (b) 60 krpm, (c) 120 krpm.

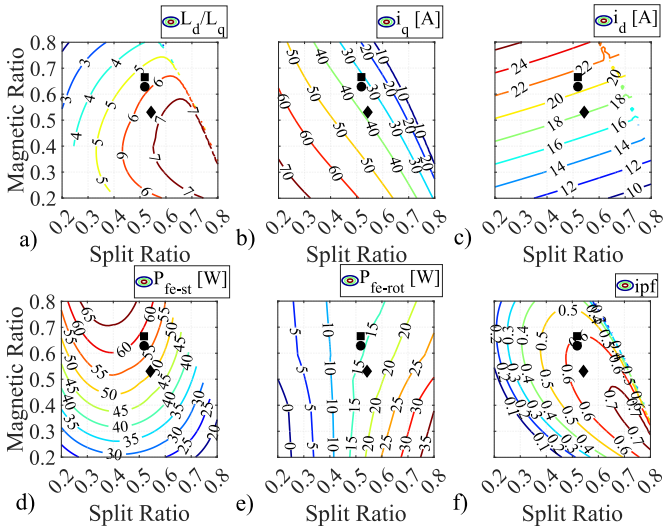

Fig. 9. Constant loci at 60 krpm obtained considering only the losses effect. L_d/L_q (a), i_q (b), i_d (c), P_{fe-st} (d), P_{fe-rot} (e), ipf (f).

q-axis inductance than on the torque as shown in Fig. 10d and 10e. The latter report the percentage variations of torque and q-axis inductance worsening always for the 60 krpm case with respect to the design with no ribs. The high increase of the q-axis inductance causes a significant power factor drop, as reported in Fig. 10f.

This analysis allows drawing the following considerations.

- The presence of the structural iron ribs reduces the optimal split ratio and increases the optimal magnetic ratio since this design direction allows to minimize $\Delta L_{q-rib}[\%]$ and so $\Delta T_{rib}[\%]$.
- The effect of the iron losses is that the optimum location moves toward the bottom-right of the design plane (i.e higher split ratio and lower magnetic ratio) because in the same direction the magnetic anisotropy increases and the stator iron losses decreases.
- When both iron losses and structural ribs are considered in the design exercise, the trends of the optimal split and magnetic ratios are a compromise between their competitive effects and so depend on the considered magnetic materials (as reported in Fig. 6).

C. Thermal analysis

The comparative design exercise among different lamination materials has been carried out considering the same total

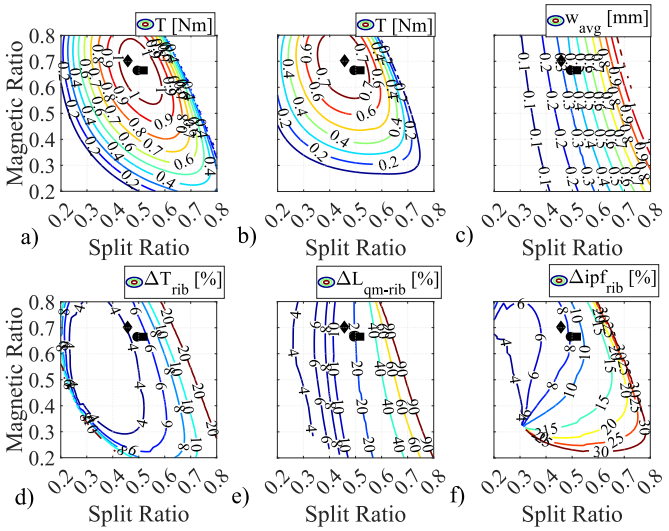

Fig. 10. Constant loci obtained considering only the ribs effect. Torque at: (a) 60 krpm, (b) 120 krpm; w_{avg} (c), ΔT_{rib} (d), ΔL_{qm-rib} (e) and Δipf_{rib} (f) at 60 krpm.

losses equal to the maximum capability of the cooling system. This assumption guarantees that the thermal behaviours of the designed machines are approximately the same avoiding the need of redesigning a new cooling system for each motor. The total loss has been imposed considering the winding Joule loss at a given temperature (i.e. 130°C) throughout the whole design process and independently from the lamination material. Although the total loss is kept constant, machines featuring the same constituent materials but different geometries (i.e. different sr, mr) or machines featuring different materials have a diverse loss distribution (copper, stator and rotor iron losses). Consequently, the temperature distribution of the compared optimal machines will not be exactly the same even though the total loss has been kept unchanged. Indeed, machines with higher Joule losses experience higher winding temperatures as these are more difficult to be extracted with respect to the stator iron losses. Fig. 11a reports the winding temperatures of the optimal machines calculated with the commercial suite [44] considering an external spiral water jacket as cooling system (whose details will be reported in the next section). Fig. 11b depicts the ratio between the Joule loss and the total stator losses. As expected, designs with higher Joule to iron loss ratio exhibit higher winding temperature.
In addition, machines designed with CoFe alloys (M4, M5) have lower copper losses with respect to the SiFe ones (M2, M3) and so they feature a lower winding temperature rise.
Fig. 11c and d show the rotor temperature and the ratio between the rotor iron loss and the total losses, respectively. Machines with mechanically optimized rotor material (M3 and M5) pay the price of higher rotor iron losses and therefore worse rotor temperature (compared to M2 and M4). Comparing solutions designed with CoFe and SiFe, the former definitely lead to higher rotor temperatures given their higher rotor iron losses.
Fig. 11e outlines the power absorbed by the cooling system for all material combinations along with the one considered during

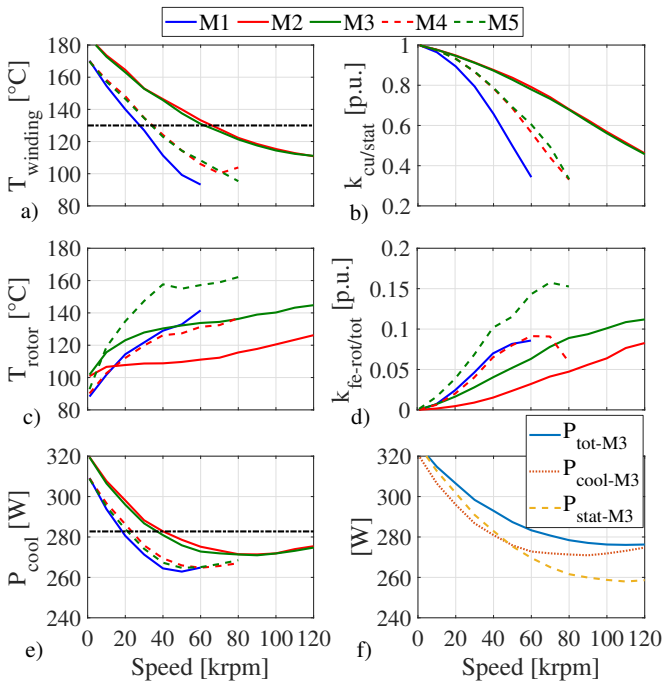

Fig. 11. a,c) Average winding and rotor temperatures, b,d) loss distribution ratios, e) total power absorbed by the cooling system of the optimal machines and f) total losses, stator total losses and cooling system power absorption for the M3 solutions.

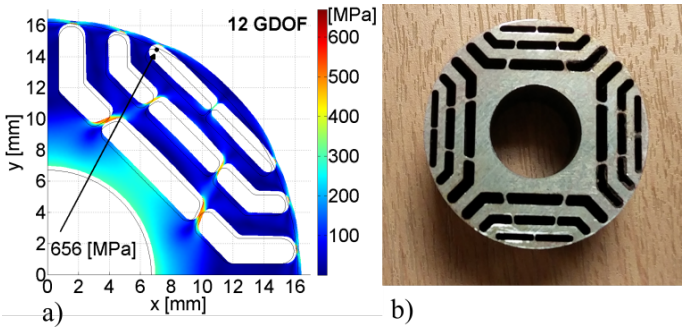

Fig. 12. a) Von Mises stress distribution of the final rotor design, b) rotor stack prior the shaft assembly.

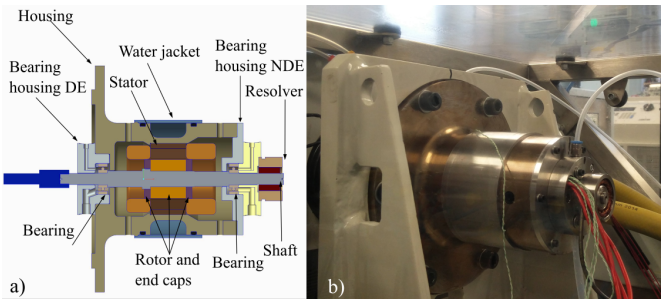

Fig. 13. a) Section drawing of the built prototype showing the most important components, b) side view of the complete machine mounted on the bracket of the test rig.

the design process (black dotted line). It can be noticed that the dissipated losses deviate from the initial value due to the different winding temperature rise, leading to different Joule losses at thermal steady state. In any case, this deviation is within 10% confirming that the comparison is performed on a fair basis as the cooling system is suitable to cover all the considered machines.

Last sub-figure (Fig. 11f) reports the loss absorbed by the cooling system for the material combination M3 along with its stator and total losses. Up to a certain speed (approximately 50 krpm) the losses absorbed by the coolant almost equal the total stator losses, while above this speed the cooling system dissipates also part of the rotor iron losses. This confirms that the calculation of the maximum current with eq.(4), considering also the rotor iron losses, is a conservative approach suitable for designing machines for a wide range of maximum speeds.

VI. Experimental Validation

To validate the proposed design approach and the considerations regarding the soft magnetic material selection, a prototype of the optimal machine at 80 krpm with the material combination M3 has been developed and tested. Before commencing the manufacturing, the rotor optimal geometry needs a structural FE refinement. In fact, the proposed design approach allows restricting the range of promising solutions, but once a geometry is chosen, its rotor needs to be structurally optimized. Indeed, the distribution of the iron ribs along the barriers have to be optimized trying to keep the total iron bridge thickness per barrier as close as possible to the analytical estimated values. By doing so, the average torque would not change being not affected by the ribs position along the barrier but mainly by their thickness. A comprehensive description of the adopted structural design procedure is reported in [45], while Fig. 12 reports the Von Mises stress distribution of the final rotor geometry along with the photo of the EDM manufactured rotor lamination stack prior the shaft and end-caps assembly.

Fig. 13 shows a section view of the overall prototype highlighting the main components along with a photo of the assembled system. The cooling system consists in a single spiral water jacket covering the whole stator axial length with a rated flow rate of 20 litre/min [27]. The same figure also depicts the bearing housing featuring inlet and outlet channels for the air-oil mist lubrication of the selected bearings.

The prototyped SyR machine was coupled, via a gearbox (ratio 1:5.975) and a 3.5 Nm torque sensor, to a load motor (37 kW - 20 krpm IM) supplied with a four-quadrant regenerative drive. An in-house designed three-phase full-bridge converter featuring SiC power modules has been used to supply the machine under test. The control platform used to implement the control algorithm is based on a Xilinx Zynq7020 SoC. A high ratio between the switching and the fundamental frequency was guaranteed setting the switching frequency to 40 kHz.

To confirm the FE-calculated performance and implement an accurate vector control, the flux–current relationships of the SyR prototype have been identified adopting the procedure presented in [46]. Fig. 14 reports the results of this experimental identification over the entire d-q current plane with a satisfactory agreement with the FE prediction.

After measuring the d- and q-axis fluxes, it is possible

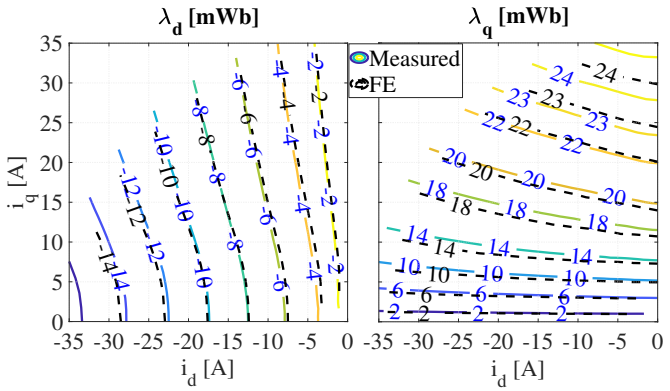

Fig. 14. Comparison between measured and FE d- and q-axis fluxes in the d-q current plane.

to derive the torque and inductances along the maximum torque per ampere trajectory needed to tune and implement the standard vector control scheme. After some preliminary tests, several motoring no-load tests have been performed imposing a trapezoidal speed reference with increasing maximum values. Fig. 15 reports the measured and the reference speed, d- and q-axis currents and reference voltages during a no-load test up to 35 krpm. After verifying the safe operations up to a certain speed, an extensive campaign of generating load tests has been performed at different speeds and loads.

For every considered speed and load (up to 30 krpm at full load, 28A), the tests were carried out reaching the thermal steady state and acquiring several electrical, mechanical and thermal variables. Fig. 16 shows the transient behaviour of the speed, torque, voltage and currents (in the d-q reference frame) during the current step between 21 and 28 A at 30 krpm. The same figure also reports the steady state phase currents, dc link voltage, duty cycles and torque. This condition correspond to the machine producing the rated torque ($T_{rated} = 0.77Nm$).

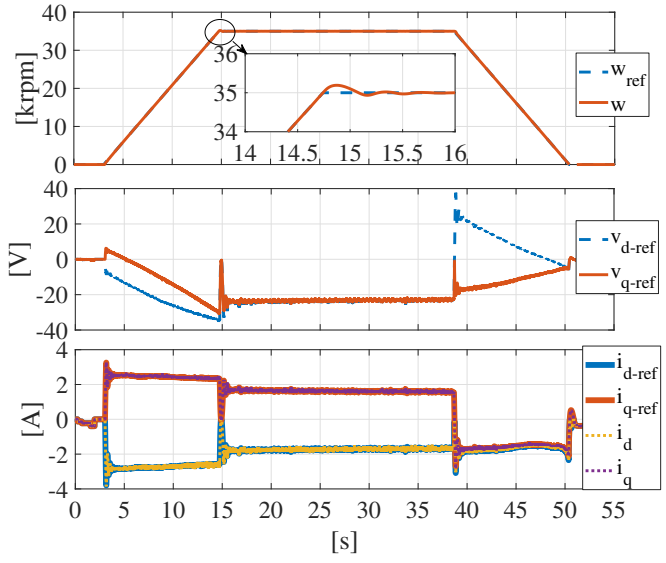

Fig. 15. Measured and reference speeds, voltage reference and measured and reference currents during a motoring no-load test.

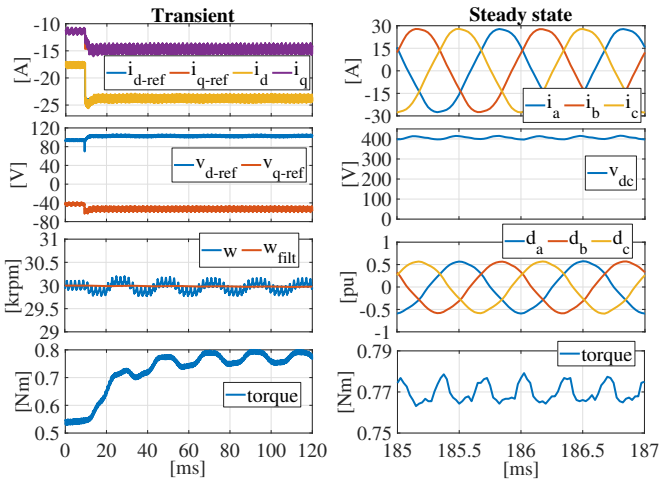

Fig. 16. Transient and steady state acquisitions during the load test at 30 krpm in which the current module increases from 21 to 28 A.

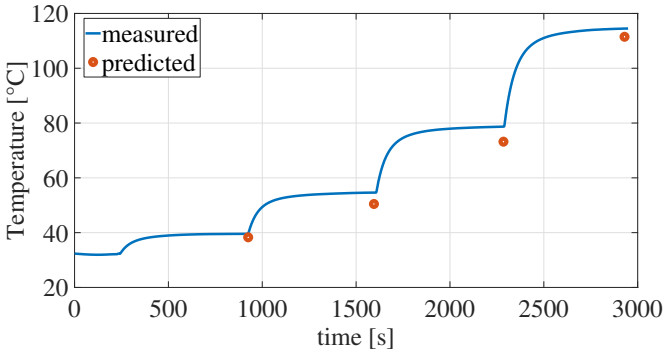

Fig. 17. Measured winding temperature during the load tests at 30 krpm compared with the estimated ones at steady state.

Above 30krpm (at load) and 35krpm (at no load), the measured vibrations exceeds the acceptable limits and, for the sake of safety, tests at higher speed have not been performed. An in depth analysis of the vibration spectrum at the different rotating speeds leads to the conclusion that a shaft misalignment (or a non-perfect alignment of the bearings within their housings) is the most probable cause of this behaviour.

The last figure (Fig. 17) outlines the measured temperatures experienced by the winding during the load tests (with torques from $^1/_4T_{rated}$ to the rated value with a step of $^1/_4T_{rated}$) at 30 krpm. The thermal model used during the comparative design exercise described in Section V-C has been used to estimate the thermal performance of the prototyped machines at 30 krpm and the rated torque. The average winding temperature predictions, also shown in Fig. 17, are underestimated (about 10%) with respect to the measured ones.

VII. Conclusion

This paper has presented a hybrid design approach for synchronous reluctance machines suitable for high speed operation. Magnetic non-linearity, rotor structural limitation and the rise of iron losses have been carefully considered weighing their competitive effects.

After FE-validating the proposed approach, a comparative design exercise, investigating different soft magnetic materials, has been presented.

The analysis showed that adopting CoFe alloys leads to machines that outperform the SiFe counterpart up to a certain speed, which for the considered case study is about 60 krpm. Above this speed, machines with SiFe provide better performance. In the lower speed range, the effect of the higher saturation flux density of the CoFe alloys allows achieving better performance. On the contrary, for higher design speeds, the higher iron losses and low yield strength of the CoFe materials outweigh the advantage of the higher saturation level and make the SiFe adoption more convenient. Using materials (either SiFe or CoFe) with a higher yield strength for the rotor, always leads to better performance despite their higher iron losses. The analysis of the optimal machines showed that the split ratio and magnetic loads decrease as the speed increases with a higher decrement rate when adopting materials with low yield strength for the rotor.

The thermal analysis of the same set of machines has confirmed the validity of the implemented design approach. In particular, keeping invariant the total machine losses for all the design speeds allows a comparison on a fair basis, i.e. with the same cooling system. Although the distribution of the losses varies as the design speed increases, the maximum winding temperatures of all designs lie within an acceptable range, indeed.

Several experimental tests on a 6.5kW-80krpm SyR machine have been reported endorsing all the design considerations. Different mechanical limitations have constrained the maximum speed during the experimental tests up to 30 krpm. Nonetheless, the reported experimental results up to the rated current fully validate the proposed design methodology.

REFERENCES

[1] A. Krings, A. Boglietti, A. Cavagnino, and S. Sprague. Soft magnetic material status and trends in electric machines. *IEEE Transactions on Industrial Electronics*, 64(3):2405–2414, 2017.

[2] N. Fernando, G. Vakil, P. Arumugam, E. Amankwah, C. Gerada, and S. Bozhko. Impact of soft magnetic material on design of high-speed permanent-magnet machines. *IEEE Transactions on Industrial Electronics*, 64(3):2415–2423, 2017.

[3] D. Golovanov, D. Gerada, G. Sala, M. Degano, A. Trentin, P. H. Connor, Z. Xu, A. La Rocca, A. Galassini, L. Tarisciotti, C. N. Eastwick, S. J. Pickering, P. Wheeler, J. C. Clare, M. Filipenko, and C. Gerada. 4mw class high power density generator for future hybrid-electric aircraft. *IEEE Transactions on Transportation Electrification*, pages 1–1, 2021.

[4] L. Shao, A. E. H. Karci, D. Tavernini, A. Sorniotti, and M. Cheng. Design approaches and control strategies for energy-efficient electric machines for electric vehicles—a review. *IEEE Access*, 8:116900–116913, 2020.

[5] A. Krings, M. Cossale, A. Tenconi, J. Soulard, A. Cavagnino, and A. Boglietti. Magnetic materials used in electrical machines: A comparison and selection guide for early machine design. *IEEE Industry Applications Magazine*, 23(6):21–28, 2017.

[6] M. Cossale, A. Krings, J. Soulard, A. Boglietti, and A. Cavagnino. Practical investigations on cobalt–iron laminations for electrical machines. *IEEE Transactions on Industry Applications*, 51(4):2933–2939, 2015.

[7] O. Bottauscio, G. Serra, M. Zucca, and M. Chiampi. Role of magnetic materials in a novel electrical motogenerator for the more electric aircraft. *IEEE Transactions on Magnetics*, 50(4):1–4, 2014.

[8] M. A. Prabhu, J. Y. Loh, S. C. Joshi, V. Viswanathan, S. Ramakrishna, C. J. Gajanayake, and A. K. Gupta. Magnetic loading of soft magnetic material selection implications for embedded machines in more electric engines. *IEEE Transactions on Magnetics*, 52(5):1–6, 2016.

[9] M. Centner and U. Schafer. Optimized design of high-speed induction motors in respect of the electrical steel grade. *IEEE Transactions on Industrial Electronics*, 57(1):288–295, 2010.

[10] E. C. Lovelace, T. M. Jahns, T. A. Keim, and J. H. Lang. Mechanical design considerations for conventionally laminated, high-speed, interior pm synchronous machine rotors. *IEEE Transactions on Industry Applications*, 40(3):806–812, 2004.

[11] A. Credo and P. Pescetto. Design optimization of a synchronous reluctance motor based on operating cycle. In *2020 International Conference on Electrical Machines (ICEM)*, volume 1, pages 2486–2492, 2020.

[12] M. Salameh, I. P. Brown, and M. Krishnamurthy. Fundamental evaluation of data clustering approaches for driving cycle-based machine design optimization. *IEEE Transactions on Transportation Electrification*, 5(4):1395–1405, 2019.

[13] Shafigh Nategh, Aldo Boglietti, Yujing Liu, Daniel Barber, Ron Brammer, David Lindberg, and Ola Aglen. A review on different aspects of traction motor design for railway applications. *IEEE Transactions on Industry Applications*, 56(3):2148–2157, 2020.

[14] H. Fujimura R. Hirayama K. Wajima S. Yamazaki. Non-oriented electrical steel sheet and its application technology for the traction motors of hybrid/electrical vehicles. *Nipponn Steel Technical Report No. 122 November 2019*.

[15] A. T. de Almeida, F. J. T. E. Ferreira, and G. Baoming. Beyond induction motors—technology trends to move up efficiency. *IEEE Transactions on Industry Applications*, 50(3):2103–2114, May 2014.

[16] Seyedmorteza Taghavi and Pragasen Pillay. A sizing methodology of the synchronous reluctance motor for traction applications. *IEEE Journal of Emerging and Selected Topics in Power Electronics*, 2(2):329–340, 2014.

[17] P. Ramesh and N. C. Lenin. High power density electrical machines for electric vehicles—comprehensive review based on material technology. *IEEE Transactions on Magnetics*, 55(11):1–21, 2019.

[18] A. Credo, G. Fabri, M. Villani, and M. Popescu. Adopting the topology optimization in the design of high-speed synchronous reluctance motors for electric vehicles. *IEEE Transactions on Industry Applications*, 56(5):5429–5438, 2020.

[19] Yi Wang, Dan M. Ionel, and David Staton. Ultrafast steady-state multiphysics model for pm and synchronous reluctance machines. *IEEE Transactions on Industry Applications*, 51(5):3639–3646, 2015.

[20] Seyed Morteza Taghavi and Pragasen Pillay. A mechanically robust rotor with transverse laminations for a wide-speed-range synchronous reluctance traction motor. *IEEE Transactions on Industry Applications*, 51(6):4404–4414, 2015.

[21] M. N. Ibrahim, Peter Sergeant, and E. M. Rashad. Synchronous reluctance motor performance based on different electrical steel grades. *IEEE Transactions on Magnetics*, 51(11):1–4, 2015.

[22] M. Palmieri, M. Perta, F. Cupertino, and G. Pellegrino. High-speed scalability of synchronous reluctance machines considering different lamination materials. In *IECON 2014 - 40th Annual Conference of the IEEE Industrial Electronics Society*, pages 614–620, 2014.

[23] C. Babetto, G. Bacco, and N. Bianchi. Analytical power limits curves of high-speed synchronous reluctance machines. *IEEE Transactions on Industry Applications*, 55(2):1342–1350, 2019.

[24] A. Vagati, G. Franceschini, I. Marongiu, and G. P. Troglia. Design criteria of high performance synchronous reluctance motors. In *Industry Applications Society Annual Meeting, 1992., Conference Record of the 1992 IEEE*, pages 66–73 vol.1.

[25] S. Ferrari and G. Pellegrino. Feafix: Fea refinement of design equations for synchronous reluctance machines. *IEEE Transactions on Industry Applications*, 56(1):256–266, 2020.

[26] Gianvito Gallicchio, Mauro Di Nardo, Marco Palmieri, Alessandro Marfoli, Michele Degano, Chris Gerada, and Francesco Cupertino. High speed synchronous reluctance machines: Modeling, design and limits. *IEEE Transactions on Energy Conversion*, pages 1–1, 2021.

[27] Mauro Di Nardo. *Design of High Speed Synchronous Reluctance Machine*. PhD thesis, University of Nottingham, UK, 2017.

[28] F. Cupertino *et al.* "Synchronous Reluctance (machines) - evolution". Accessed: Dec. 18, 2020. [Online]. Available: https://sourceforge.net/projects/syr-e/.

[29] W. Lee, E. Schubert, Y. Li, S. Li, D. Bobba, and B. Sarlioglu. Overview of electric turbocharger and supercharger for downsized internal combustion engines. *IEEE Transactions on Transportation Electrification*, 3(1):36–47, 2017.

[30] C. Babetto, G. Bacco, and N. Bianchi. Synchronous reluctance machine optimization for high-speed applications. *IEEE Transactions on Energy Conversion*, 33(3):1266–1273, 2018.

[31] J. B. Bartolo, Zhang He, D. Gerada, L. de Lillo, and C. Gerada. High speed electrical generators, application, materials and design. In *Electrical Machines Design Control and Diagnosis (WEMDCD), 2013 IEEE Workshop on*, pages 47–59.
[32] S. Sprague. Emerf lamination steels (3rd ed.). [cd-rom]. Motion Control and Motor, Ann Arbor, MI, 2009.
[33] "VAC Vacuumschmelze". Accessed: Feb. 22, 2021. [Online]. Available: https://www.vacuumschmelze.com.
[34] "JFE Steel Corporation". Accessed: Feb. 22, 2021. [Online]. Available: https://www.jfe-steel.co.jp/enm.
[35] "Nippon Steel and Sumitomo Metal". Accessed: Feb. 22, 2021. [Online]. Available: https://www.nssmc.com.
[36] D. Gerada, A. Mebarki, N. L. Brown, C. Gerada, A. Cavagnino, and A. Boglietti. High-speed electrical machines: Technologies, trends, and developments. *Industrial Electronics, IEEE Transactions on*, 61(6):2946–2959, 2014.
[37] Darja Steiner Petrovic. Non-oriented electrical steel sheets. *Materials and Technologies*, 44:317–325, 11 2010.
[38] Yoshihiko Oda, Masaaki Kohno, and Atsuhito Honda. Recent development of non-oriented electrical steel sheet for automobile electrical devices. *Journal of Magnetism and Magnetic Materials*, 320(20):2430–2435, 2008. Proceedings of the 18th International Symposium on Soft Magnetic Materials.
[39] Kim Verbeken, Ivone Infante Danzo, J Barros-Lorenzo, Jürgen Schneider, and Yvan Houbaert. Innovative processing for improved electrical steel properties. *Revista de Metalurgia*, 46(5):458–468, 2010.
[40] Senda Kunihiro Namikawa Misao Hayakawa Yasuyuki. Electrical steels for advanced automobiles—core materials for motors, generators, and high-frequency reactors. *Jfe Technical Report No. 4 (Nov. 2004)*.
[41] I. Tanaka and H. Yashiki. Magnetic and mechanical properties of newly developed high-strength nonoriented electrical steel. *IEEE Transactions on Magnetics*, 46(2):290–293, 2010.
[42] K. Bourchas, A. Stening, J. Soulard, A. Broddefalk, M. Lindenmo, M. Dahlén, and F. Gyllensten. Quantifying effects of cutting and welding on magnetic properties of electrical steels. *IEEE Transactions on Industry Applications*, 53(5):4269–4278, 2017.
[43] A. Boglietti, A. Cavagnino, L. Ferraris, and M. Lazzari. The annealing influence onto the magnetic and energetic properties in soft magnetic material after punching process. In *IEEE International Electric Machines and Drives Conference, 2003. IEMDC'03.*, volume 1, pages 503–508 vol.1, 2003.
[44] "Motor-CAD". Accessed: Jan. 11, 2021. [Online]. Available: https://www.motor-design.com.
[45] M. Di Nardo, G. L. Calzo, M. Galea, and C. Gerada. Structural design optimization of a high speed synchronous reluctance machine. In *2016 XXII International Conference on Electrical Machines (ICEM)*, pages 2073–2079, Sept 2016.
[46] E. Armando, R. I. Bojoi, P. Guglielmi, G. Pellegrino, and M. Pastorelli. Experimental identification of the magnetic model of synchronous machines. *Industry Applications, IEEE Transactions on*, 49(5):2116–2125, 2013.

Mauro Di Nardo (M'18) received the M.Sc. (Hons.) degree in electrical engineering from the Polytechnic University of Bari, Italy, in 2012, and the Ph.D. degree in electrical machine design from the University of Nottingham, U.K., in 2017. From 2017 to 2019, he was Head with the AROL R&D Team within the Polytechnic University of Bari leading industrial projects on electrical drives design for mechatronics applications.

Since the 2019, he is with the Power Electronics and Machine Control Group of the University of Nottingham as Research Fellow working on wide variety of projects. His research interests include the analysis, modelling, and design optimizations of permanent magnet and synchronous reluctance machines for automotive, aerospace and household sectors, induction motor for industrial applications as well as niche machine topologies such as bearingless and hysteresis motor.

He has been serving as an Associate Editor for the Open Journal of Industry Applications since March 2021.

Gianvito Gallicchio received the B.Sc. (Hons.) and M.Sc. (Hons.) degrees in electrical engineering from the Politecnico di Bari, Bari, Italy, in 2016 and 2018, respectively. He is currently working toward the Ph.D. degree with the Electrical Machines and Drives Group, Politecnico di Bari, Bari, Italy.

His main research interests include the analysis, modelling and design of magnetic couplers for industrial applications and the design of electrical machines, including permanent magnet and synchronous reluctance machines, for aerospace sector.

Marco Palmieri received the M.Sc. and Ph.D. degrees in electrical engineering from Politecnico di Bari, Bari, Italy, in 2011 and 2016, respectively. Since 2017 he has been with the Department of Electrical and Information Engineering, Politecnico di Bari, where he is currently a post-doc researcher.

From 2011 to 2015, he was with the Energy Factory Bari Research Team, working on high-speed electrical machines for aeronautical applications. In 2014 he joined the Power Electronics, Control, and Machines Research Group of the University of Nottingham, working on electrical machines for aeronautical applications. In 2019 he was visiting researcher with the Laboratory of Actuation Technology of the Saarland University. His research interests include the design of high-speed electrical machines by means of optimization algorithms and finite element analysis.

Dr. Palmieri co-received the Prize Paper Award from the IEEE Industrial Electronics Society Electrical Machines Committee in 2015.

Alessandro Marfoli received the M.Sc. in Electrical Engineering from the University of Pisa, Italy, in 2015 and the Ph.D. degree in electrical machine design from the University of Nottingham (UK) in 2020. He is currently a Research Fellow within the same institution working on wide variety of projects of high industrial and scientific impacts.

His main research interests involves the modelling, analysis and optimization of electrical machines including induction and synchronous machines also for bearingless applications.

Michele Degano (SM'21) received his Master's degree in Electrical Engineering from the University of Trieste, Italy, in 2011, and his Ph.D. degree in Industrial Engineering from the University of Padova, Italy, in 2015. Between 2014 and 2016, he was a postdoctoral researcher at The University of Nottingham, UK, where he joined the Power Electronics, Machines and Control (PEMC) Research Group. In 2016 he was appointed Assistant Professor in Advanced Electrical Machines, at The University of Nottingham, UK. He was promoted Associate Professor in 2020.

His main research focuses on electrical machines and drives for industrial, automotive, railway and aerospace applications, ranging from small to large power.

He is currently the PEMC Director of Industrial Liaison leading research projects for the development of hybrid electric aerospace platforms and electric transports.

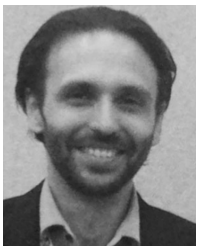

Giovanni Lo Calzo received the master's degree (with Hons.) and Ph.D. degree from the University of Roma Tre, Rome, Italy, in 2010 and 2015, respectively. From 2010 to 2011, he was a Research Assistant with the University of Roma Tre, while in 2015, he joined the Power Electronics, Machine and Control Group, University of Nottingham, Nottingham, U.K., as Research Fellow, focusing on the modeling, design, and control of power electronics converters.

In 2017, he moved to Dyson Ltd., within its innovative EV development program. Since 2018, he has been with the Ferrari S.p.A., Maranello, Italy, as a Team Leader for the design of power electronics components in the Hybrid Components Department.

Chris Gerada (SM'12) is an Associate Pro-Vice-Chancellor for Industrial Strategy and Impact and Professor of Electrical Machines. His principal research interest lies in electromagnetic energy conversion in electrical machines and drives, focusing mainly on transport electrification. He has secured over £20M of funding through major industrial, European and UK grants and authored more than 350 referred publications. He received the Ph.D. degree in numerical modelling of electrical machines from The University of Nottingham, Nottingham, U.K., in 2005. He subsequently worked as a Researcher with The University of Nottingham on high-performance electrical drives and on the design and modelling of electromagnetic actuators for aerospace applications. In 2008, he was appointed as a Lecturer in electrical machines; in 2011, as an Associate Professor; and in 2013, as a Professor at The University of Nottingham. He was awarded a Research Chair from the Royal Academy of Engineering in 2013.

Prof. Gerada served as an Associate Editor for the IEEE TRANSACTIONS ON INDUSTRY APPLICATIONS and is the past Chair of the IEEE IES Electrical Machines Committee.

Francesco Cupertino (M'08–SM'12) received the Laurea and Ph.D. degrees in electrical engineering from the Politecnico di Bari, Bari, Italy, in 1997 and 2001, respectively. Since 2001, he has been with the Department of Electrical and Information Engineering, Politecnico di Bari, Bari, Italy, where he is currently a Full Professor of converters, electrical machines, and drives.

He is the Scientific Director of four public/private laboratories at Politecnico di Bari that enroll more than 50 researchers; the laboratory Energy Factory Bari, with GE AVIO, aimed at developing research projects in the fields of aerospace and energy; the More Electric Transportation laboratory, with CVIT SpA (BOSCH Group), aimed at developing technologies for sustainable mobility; Cyber Physical Systems AROL Bari, with AROL SpA, focused on closure systems for food and beverage; Innovation for Mills, with Casillo Group and Idea75, focused in the Industry4.0 applications for wheat processing. He has authored or coauthored more than 130 scientific papers on these topics. His research interests include the design of synchronous electrical machines, motion control of high performances electrical machines, applications of computational intelligence to control, and sensorless control of ac electric drives.

Dr. Cupertino was the recipient of two Best Paper Awards from the Electrical Machines Committee of the IEEE Industry Application Society and from the homonymous Committee of the IEEE Industrial Electronics Society, in 2015.

He is currently the rector of Politecnico di Bari.